

RESEARCH ARTICLE

Study on 3D printing process of continuous polyglycolic acid fiber-reinforced polylactic acid degradable composites

Patiguli Aihemaiti[†], Ru Jia[†], Wurikaixi Aiyiti^{*}, Houfeng Jiang, Ayiguli Kasimu

School of Mechanical Engineering, Xinjiang University, Urumqi 830000, PR China

Abstract

A continuous polyglycolic acid (PGA) fiber-reinforced polylactic acid (PLA) degradable composite was proposed for application in biodegradable load-bearing bone implant. The fused deposition modeling (FDM) process was used to fabricate composite specimens. The influences of the printing process parameters, such as layer thickness, printing spacing, printing speed, and filament feeding speed on the mechanical properties of the PGA fiber-reinforced PLA composites, were studied. The thermal properties of the PGA fiber and PLA matrix were investigated by using differential scanning calorimetry (DSC) and thermogravimetric analysis (TGA). The internal defects of the as-fabricated specimens were characterized by the micro-X-ray 3D imaging system. During the tensile experiment, a full-field strain measurement system was used to detect the strain map and analysis the fracture mode of the specimens. A digital microscope and field emission electron scanning microscopy were used to observe the interface bonding between fiber and matrix and fracture morphologies of the specimens. The experimental results showed that the tensile strength of specimens was related to their fiber content and porosity. The printing layer thickness and printing spacing had significant impacts on the fiber content. The printing speed did not affect the fiber content but had a slight effect on the tensile strength. Reducing the printing spacing and layer thickness could increase the fiber content. The tensile strength (along the fiber direction) of the specimen with 77.8% fiber content and 1.82% porosity was the highest, reaching 209.32 ± 8.37 MPa, which is higher than the tensile strength of the cortical bone and polyether ether ketone (PEEK), indicating that the continuous PGA fiber-reinforced PLA composite has great potential in the manufacture of biodegradable load-bearing bone implants.

Keywords: 3D printing; Continuous fiber-reinforced composites; Biodegradable implants; Mechanical properties

[†]These authors contributed equally to this work.

***Corresponding author:**
Wurikaixi Aiyiti
(wurikaixi@xju.edu.cn)

Citation: Aihemaiti P, Jia R, Aiyiti W, et al., 2023, Study on 3D printing process of continuous polyglycolic acid fiber-reinforced polylactic acid degradable composites. *Int J Bioprint*.
<https://doi.org/10.18063/ijb.734>

Received: December 07, 2022
Accepted: March 07, 2023
Published Online: April 19, 2023

Copyright: © 2023 Author(s). This is an Open Access article distributed under the terms of the Creative Commons Attribution License, permitting distribution, and reproduction in any medium, provided the original work is properly cited.

Publisher's Note: Whioce Publishing remains neutral with regard to jurisdictional claims in published maps and institutional affiliations.

1. Introduction

The combination of three-dimensional (3D) printing technology and advanced design technologies, such as reverse engineering, computer-aided design (CAD), topology optimization design, has very obvious advantages in the field of customized load-bearing bone implant manufacturing^[1-4]. Load-bearing implants are commonly fabricated with metal materials such as titanium^[5,6] and tantalum^[7,8] or high-performance polymers

like polyether ether ketone (PEEK)^[9,10] due to their excellent mechanical properties and biocompatibility. However, metal materials have mismatching elastic modulus with human bone, and PEEK material shows inherent bioinert property and hydrophobicity^[11]. More importantly, these materials are non-biodegradable, which limits their clinical application in degradable load-bearing implant applications^[12]. Polylactic acid (PLA), a biodegradable polymer, has been used to form non-load-bearing orthopedic implants (such as degradable bone plates and screws) and tissue engineering scaffolds due to their admirable attributes in terms of biocompatibility, biodegradability, and biosafety^[13-15]. However, the applications of PLA in load-bearing implant have been restricted due to its poor mechanical properties.

Adding the particle, short fiber, and continuous fiber into the PLA matrix to prepare composite parts through the fused deposition modeling (FDM), 3D printing process is an effective way to improve the mechanical properties of pure PLA parts^[16-18]. Bioactive particles such as hydroxyapatite (HA) and β -tricalcium phosphate (β -TCP) have been added to the PLA to enhance the mechanical properties and bioactivity of the printed parts^[19,20]. Aihemaiti *et al.*^[21] fabricated HA-PLA composite bone plates and investigated the effect of printing parameters on the mechanical properties. Zhang *et al.*^[22] and Wang *et al.*^[23] prepared polylactic acid/nano hydroxyapatite (PLA/nHA) composite scaffolds with different loading of nHA by FDM, and the effect of the nHA ratio on the mechanical properties of the scaffolds were studied. However, these study results showed that the addition of HA particles has a limited effect on the improvement of mechanical properties. Even more, the high content of HA particles decreased the part's strength because the particles could easily aggregate and bubbles were introduced in the filaments. Therefore, the particle-reinforced PLA composite parts cannot meet the mechanical property requirement of the load-bearing implant. In addition, using short or continuous carbon fibers^[24,25], glass fibers^[26,27], flax fibers^[28,29], and kevlar fibers^[30] to reinforce PLA parts through the FDM process has been developed as an efficient way of enhancing mechanical properties of parts. Among them, the mechanical properties of the FDM-printed short fiber-reinforced PLA parts were highly dependent on the fiber length and fiber content. However, large fiber length and high fiber content may cause nozzle clogging^[16]; in this manner, the enhancement of mechanical properties of short fiber-reinforced parts is limited. Continuous fiber reinforcement was an effective way to increase the strength of parts^[31,32]. Maqsood *et al.*^[33] fabricated pure PLA, short carbon fiber-reinforced PLA (SCF-PLA), continuous carbon fiber-reinforced PLA

(CCF-PLA), and SCF/CCF-PLA specimens using FDM. The tensile and flexural properties of specimens were experimentally investigated, and the results showed that CCF-PLA had the highest tensile and flexural strength of 245.40 MPa and 168.88 MPa, respectively, and the specimen's strength increased by 460% (tensile strength) and 103% (flexural strength) compared to pure PLA.

Due to the line-by-line bonding and layer-by-layer stacking fabrication principle of the FDM process, the mechanical properties of CCF-PLLA parts show obvious anisotropy, with the strength along the fiber direction far larger than those along the transverse direction and layer direction^[34,35].

For biodegradable load-bearing bone implant application, both the matrix and the reinforcement should be degradable materials. Conventional carbon fiber, glass fiber, and kevlar fiber are non-degradable materials, which cannot be used in biodegradable implants. Polyglycolic acid (PGA) suture is a kind of biodegradable continuous fiber, which can be used as an ideal reinforcement for biodegradable composite parts^[36]. Takayama *et al.*^[37] fabricated short PGA fiber-reinforced PLA composites specimen by melt-mixing process, and a three-point bending test was used to estimate flexural strength and modulus. Ko *et al.*^[38] introduced PGA fibers and HA as fillers to PLA composite by using the manual fiber alignment and solution mixture solidification method. These studies suggest that the PGA fiber greatly improved the mechanical properties of neat PLA, but the fabrication process was complex. Hedayati *et al.*^[39] used biodegradable PGA suture as a continuous reinforcing fiber to enhance the mechanical properties of the poly (ϵ -caprolactone) (PCL) by an *in situ* impregnation FDM method. The tensile strength and elastic modulus of printed parts remarkably increased. But the effect of printing parameters on the scaffold's mechanical properties has not been studied. For the FDM process of continuous fiber-reinforced composites, many process parameters affect the mechanical properties of the printed parts^[40,41].

Our long-term research goal is to fabricate biodegradable load-bearing bone implants with tunable mechanical properties through the FDM process. In this study, PLA/PGA composite parts were fabricated by the FDM process with PGA suture as reinforcement phase and PLA wire as matrix material. The process parameters including layer thickness, printing space, printing speed, and filament feeding speed were investigated to analyze their impact on the mechanical properties of the printed specimens. The results showed that the tunable mechanical properties range was obtained by altering the printing parameters.

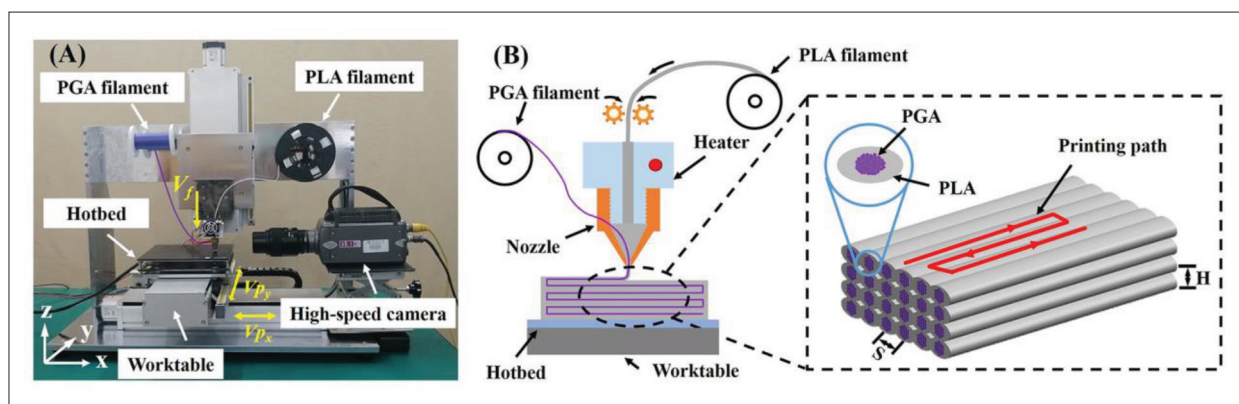


Figure 1. Experimental setup and printing principle. (A) Experimental setup and (B) printing principle. Abbreviations: PGA, polyglycolic acid; PLA, polylactic acid.

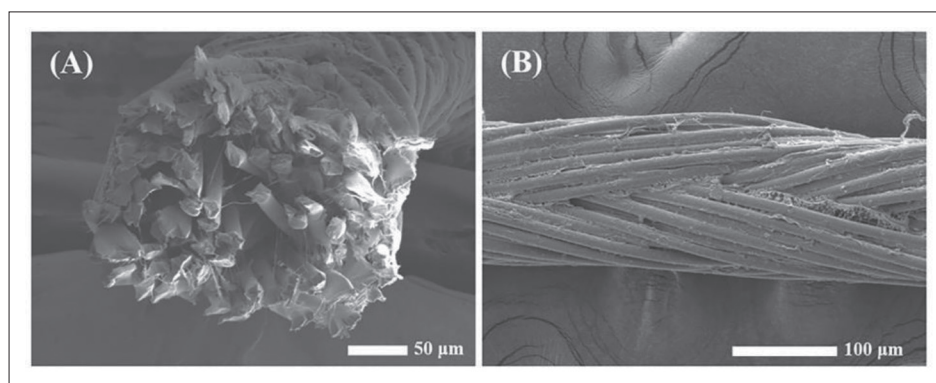


Figure 2. Morphology of polyglycolic acid (PGA) suture. (A) Section morphology and (B) surface morphology.

2. Materials and methods

2.1. Experimental setup and materials

Figure 1A shows the self-developed 3D printer for printing continuous fiber-reinforced composites. The 3D printer was driven by a three-axis closed-loop computer numerical control (CNC) system. The PLA filament was pushed into a nozzle with a heater by a filament feeder. There was a small inclined hole on the side of the nozzle, which was the channel for the PGA fiber to enter the nozzle. The PGA fiber was wrapped by the molten PLA in the nozzle, extruded from the nozzle under the pressure of the material pushed into the nozzle from the filament inlet, and deposited on the hotbed. A high-speed camera was set on the side of the worktable to observe the deposition process of the material extruded from the nozzle. The printing principle is illustrated in Figure 1B.

A PLA filament with a diameter of 1.75 mm was used as the matrix material. The reinforcing fiber was a PGA medical absorbable suture (Shandong Boda medical supplies Co., Ltd. China), with a diameter of 0.15 mm. The cross-sectional and surface morphology of the PGA suture were observed using a scanning electron microscope,

as shown in Figure 2. This PGA suture was made up of bundles of fine woven fibers.

2.2. Specimen fabrication

The process parameters studied in this work include layer thickness (H), printing spacing (S), printing speed (V_p), and filament feeding speed (V_f). Through the pre-experiment, the process parameters that can lead to fiber breakage, nozzle clogging, and very poor printing quality were eliminated, and the range of process parameters that can achieve continuous printing was obtained. In general, the filament feeding speed should match other main process parameters. The range of values that can be taken for filament feeding speed is small, because a very slow filament feeding speed will cause a discontinuous deposition line, and a very fast filament feeding speed will cause nozzle clogging. The values of parameters shown in Table 1 were selected based on preliminary results. Single-factor experiments were conducted to study the effects of the printing parameters on the mechanical properties of the composite specimens. All the experiments were conducted using a nozzle with an outlet diameter of 0.4 mm, a printing temperature of 210°C, and a hotbed temperature of 40°C.

Table 1. Parameters values

Scheme no.	Layer thickness (H , mm)	Printing spacing (S , mm)	Printing speed (V_p , mm/s)	Feeding speed (V_f , mm/s)
1	0.15	0.3	9	0.1
2	0.2	0.3	9	0.1
3	0.25	0.3	9	0.1
4	0.15	0.25	9	0.1
5	0.15	0.4	9	0.1
6	0.2	0.4	7	0.2
7	0.2	0.4	8	0.2
8	0.2	0.4	9	0.2

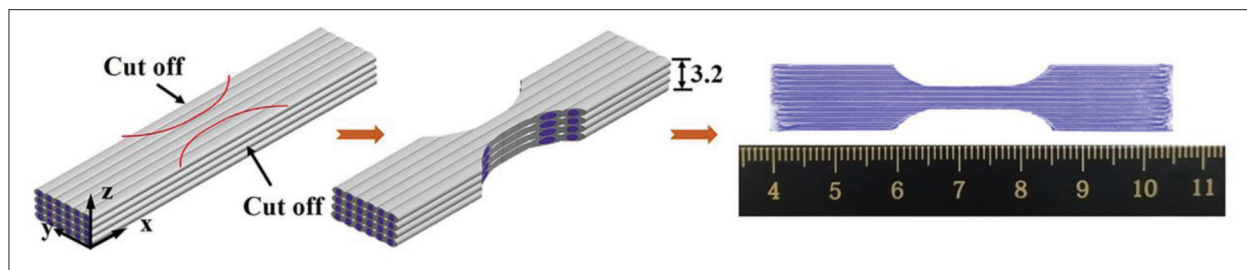


Figure 3. Schematic diagram of a tensile specimen.

Tensile specimens were made according to the ASTM D638-2014 Type-V tensile test standard. The direction of the tensile load was parallel to the printing direction of the deposition line. The tensile specimens were made by the process shown in Figure 3. First, the cuboid parts were printed according to the scheme shown in Table 1. Then, the dumbbell-shaped specimens were cut out by a special cutting guide plate. This method could ensure the integrity and continuity of the deposition line and reduce the number of printing defects of the specimens. If the tensile specimens were directly printed, the middle part of the dumbbell-shaped specimens would lead to discontinuity of the deposition line, and the possibility of defects at the junction of the deposition lines would increase, which would affect the experimental results. To ensure the repeatability and reliability of the experiment, for each process parameter configuration, three specimens were fabricated to conduct tensile experiments.

2.3. Property characterization

2.3.1. Thermal analysis

When a PLA filament entered the nozzle through the heater, it changed from a solid to a molten state and then was extruded from the nozzle and solidified into the solid state. A high temperature of molten PLA would improve the fluidity, make it easier to extrude from the nozzle, and facilitate the fusion between adjacent deposition lines. When the PGA fiber entered the nozzle, it was wrapped

by molten PLA, and then both materials were extruded together from the nozzle.

The temperature of molten PLA cannot make PGA fiber melt or decompose, and thus, PGA fiber cannot play a role in reinforcement. Therefore, a synchronous thermal analysis instrument (differential scanning calorimetry [DSC]/differential thermal analysis–thermogravimetry [DTA-TG], NETZSCH STA 449 F3, Germany) was used to analyze the thermal behavior of the PLA filament and PGA fiber and to determine the appropriate printing temperature range.

The samples were accurately weighed and sealed in an aluminum jar. They were then heated from room temperature to 550°C in a nitrogen atmosphere at a rate of 10°C/min. DSC provided the melt temperature and decomposition temperature of the material.

2.3.2. Tensile strength test

A universal mechanical testing machine (3005T, Shenzhen Regis Instrument Co., Ltd., China) was used to test the tensile strengths of the specimens, and the tensile rate was set at 2 mm/min. During the tensile test, a 3D full-field strain measurement system (3DFFSMS, XTOP 3D Technology (Shenzhen) Co., Ltd., China) was used to photograph and analyze the deformation and strain of all specimens, as shown in Figure 4. The surfaces of the specimens photographed by the camera were initially painted with white paint as a background and then covered

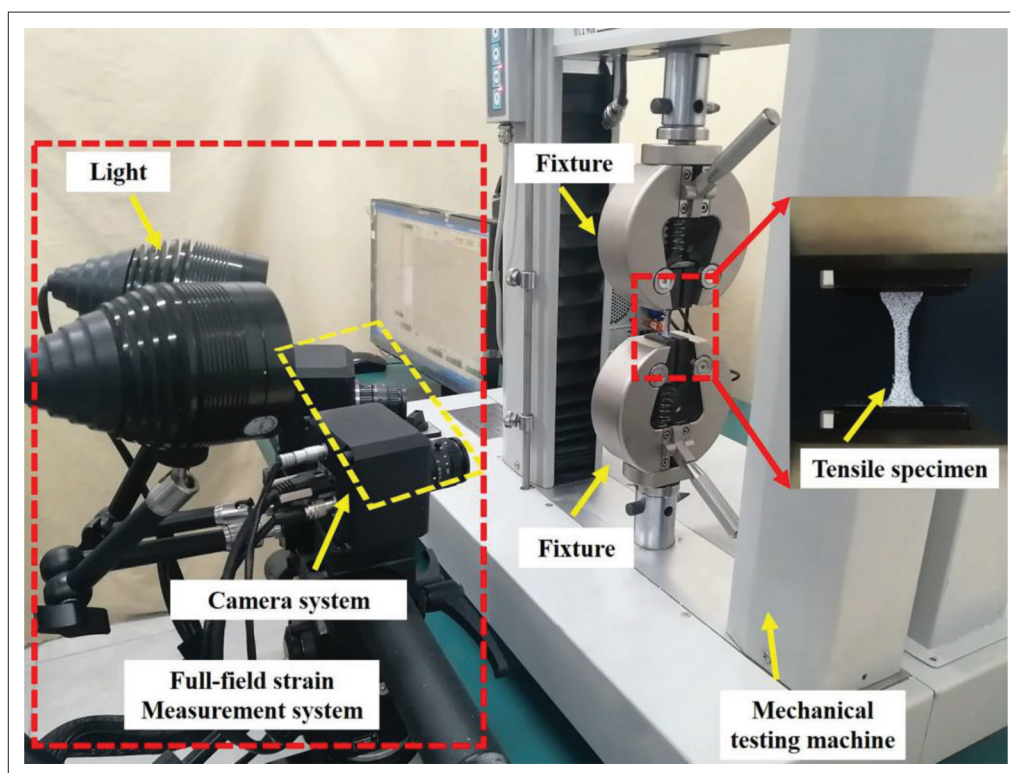


Figure 4. Experimental setup for tensile tests.

with a random pattern of black paint spots. The purpose of painting is to form scatter spots for the strain field calculation, and the thickness of paint layer is very thin and has no negative impact on the tensile strength.

2.3.3. Internal defect testing

A micro-X-ray 3D imaging system (YXLON Cheetah, Germany) was applied to analyze the internal defects of the specimens, and the internal pore geometries, volumes, and spatial distributions were also analyzed. A scan resolution of 5 μm , a peak tube potential of 80 kV, and a target current of 35 μA were set as the basic measurement parameters.

2.3.4. Analysis of printed specimen morphology

A high-speed camera (Phantom V9.1, Vision Research, Inc., USA) was used to observe the extruded material morphology of a single deposition line at different printing heights, mainly to observe the positions of the fibers in the matrix material. The capture frequency of the high-speed camera was 800 Hz. A digital microscope (VHX-6000, KEYENCE, Japan) was used to observe the cross-sectional morphology of single deposited lines and tensile specimens. Field emission electron scanning microscopy (FESEM, JSM-7610PLUS, Japan) was used to observe the cross-sections of the PLA/PGA composites and the fracture morphologies of the tensile specimens.

2.4. Statistical analysis

Group data are presented as mean \pm standard deviation. Statistical significance was determined by one-way analysis of variance (ANOVA). The significance level was set at $p < 0.01$ (**) and $p < 0.0001$ (****).

3. Results

3.1. Results of thermal analysis

The printing temperature (the temperature of the nozzle) is an important process parameter of FDM. On the one hand, it is necessary to make the molten PLA have a high temperature to ensure its good fluidity, and on the other hand, it is also necessary to ensure that the PGA fiber wrapped with PLA will not be thermally decomposed. Thermogravimetric analysis (TGA) and DSC tests were conducted to obtain the decomposition limit temperatures and melting points of the two materials, respectively, which were used to guide the selection range of the printing temperature. The TGA and DSC results of the PGA fiber and PLA materials are shown in Figure 5. The TGA curves in Figure 5A show that most of the mass (over 90%) was lost between 250°C and 390°C, and the initial decomposition temperatures of the PLA and PGA materials were 347.7°C and 306.5°C, respectively. The largest decomposition rates of the PLA and PGA materials were 28.5%/min and 21.2%/min at 367.6°C and 339.1°C,

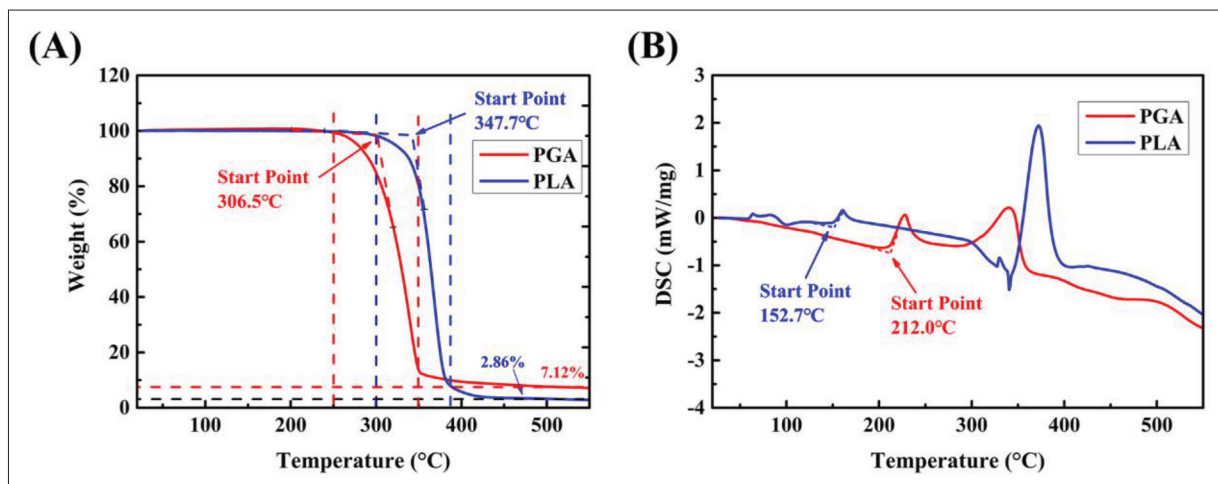


Figure 5. (A) Thermogravimetric analysis (TGA) and (B) differential scanning calorimetry (DSC) curves of polyglycolic acid (PGA) and polylactic acid (PLA).

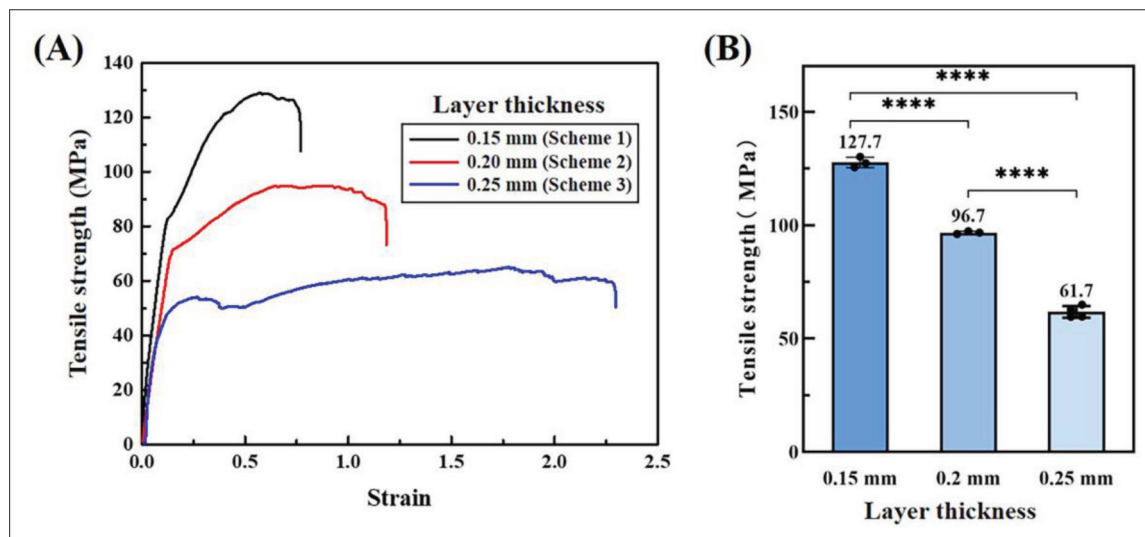


Figure 6. (A) Stress–strain curves of specimens with different layer thicknesses and (B) tensile strengths of specimens with different layer thicknesses. The tests were used to determine significant differences between groups (**** $p < 0.0001$; “•” represents the tensile test results of each specimen).

respectively. The heat flow curve in Figure 5B shows that the melting points of the PLA and PGA materials were 152.7°C and 212.0°C, respectively. From the thermal analysis results, the temperature range for PLA material printing was 152.7°C–347.7°C, and to avoid the PGA material melting, the printing temperature should be kept below 212°C. Therefore, the printing temperature was set to 210°C in this study.

3.2. Results of tensile tests

The stress–strain curves and tensile strength results for the effect of layer thickness on mechanical properties are summarized in Figures 6–8 and Table 2. The stress–strain curves of each specimen with the same process parameters

were very similar, so the average value was used to plot the stress–strain curves. Figure 6 shows the effect of the layer thickness on the tensile strength. Significant differences were found between the three printing layer thickness ($p < 0.0001$), as the layer thickness increased from 0.15 mm (scheme 1) to 0.25 mm (scheme 3), the composite specimen tensile strength decreased from 127.67 ± 2.31 MPa to 61.72 ± 2.58 MPa, decreasing by 106.9%. Figure 7 shows the effect of the printing spacing on the tensile strength. The specimens with 0.25-mm printing spacing exhibited a significant difference in tensile strength compared to the other two printing spacings. By increasing the printing space from 0.25 mm (scheme 4) to 0.40 mm (scheme 5), the tensile strength decreased from 209.32 ± 8.37 MPa to

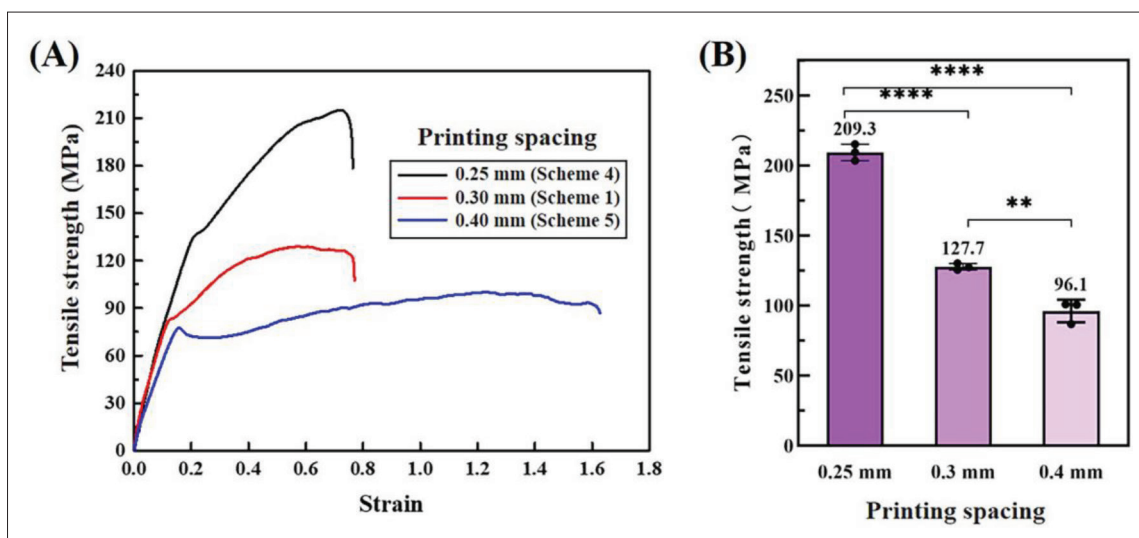


Figure 7. (A) Stress–strain curves of specimens with different printing spacings and (B) tensile strengths of specimens with different printing spacings. The tests were used to determine significant differences between groups (** $p < 0.01$, **** $p < 0.0001$; “•” represents the tensile test results of each specimen).

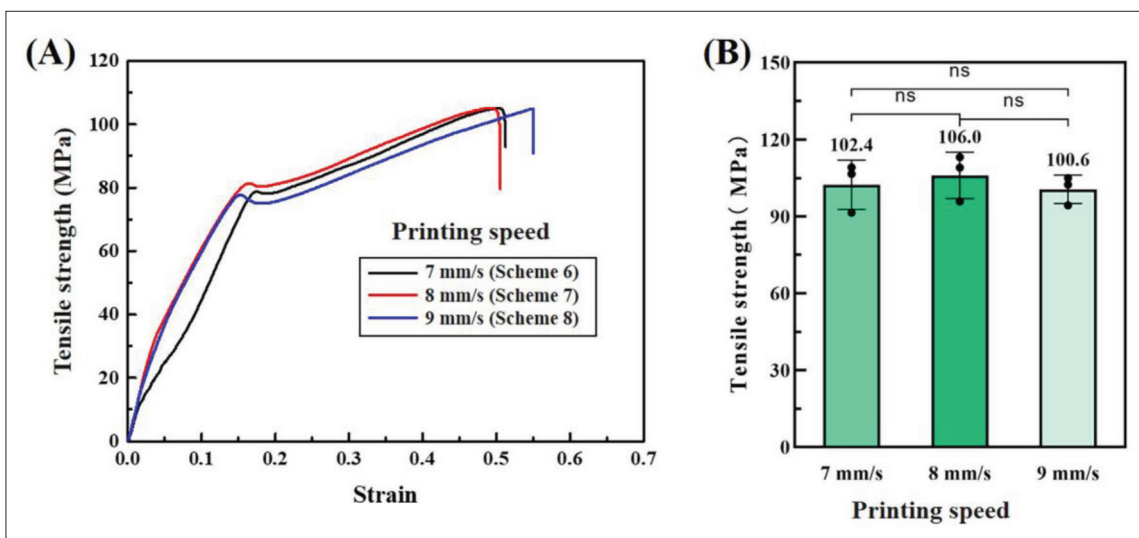


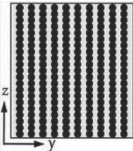
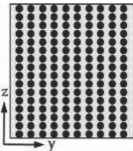
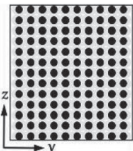
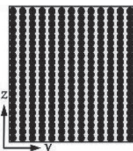
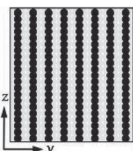
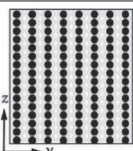
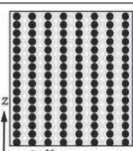
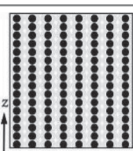
Figure 8. (A) Stress–strain curves of specimens with different printing speeds and (B) tensile strengths of specimens with different printing speeds. The tests were used to determine significant differences between groups (“ns” indicates no significance; “•” represents the tensile test results of each specimen).

96.13 ± 8.09 MPa, decreasing by 117.7%. Figure 8 shows the effect of the printing speed on the tensile strength. The tensile strength did not exhibit a significant difference among the three printing speeds.

The 3DFFSMS analysis was conducted to study the failure mode of the specimens during the tensile process. The strain cloud is the strain distribution on the specimen surface measured by 3DFFSMS. During the tensile test, the color and shape of the strain cloud change in real time, and the red area represents the area with large strain. The strain clouds corresponding to the marked points on the stress–strain curves of schemes 3, 4, and 6 and the specimens

after fracture are shown in Figure 9. Figures 9A and B show the tensile curve and fractured specimen of scheme 3, which was printed with the maximum layer thickness (0.25 mm). The specimen fracture mode of scheme 3 was quite different from those of other specimens. After the PLA matrix material was debonded from the PGA fibers, continuous single fibers worked as the main component to bear the tensile stress. No more data were collected by the 3DFFSMS after point IV on the stress–strain curve. As the tensile test continued, the internal fibers were gradually pulled off, and the printed layer was gradually debonded until the test stopped. It can be seen from Figure 9B that

Table 2. Experimental results

Scheme	Cross-section	Fiber number (Y×Z)	Fiber content (%)	Porosity (%)	Tensile strength (MPa)
1		10×21=210	59.8	3.74	127.67 ± 2.31
2		10×16=160	45.6	8.11	96.75 ± 0.87
3		10×13=130	37.0	11.48	61.72 ± 2.58
4		13×21=273	77.8	1.82	209.32 ± 8.37
5		8×21=168	47.9	4.8	96.13 ± 8.09
6		8×16=128	36.5	1.13	102.21 ± 9.46
7		8×16=128	36.5	1.35	106.01 ± 9.02
8		8×16=128	36.5	1.53	100.59 ± 5.54

many fibers leaked out from the middle of the fractured specimen, and the matrix material almost completely fell off the fibers.

The specimen of scheme 4, which was printed with the minimum printing layer thickness and printing space, had the highest tensile strength. The history of the strain

cloud during the tensile process and the specimen after the tensile failure are shown in Figures 9C and E, respectively. The tensile process of the specimen went through a linear elastic stage, a yielding stage, and an enhancement stage. A small red region appeared at point III, indicating that there is an obvious stress concentration in this small

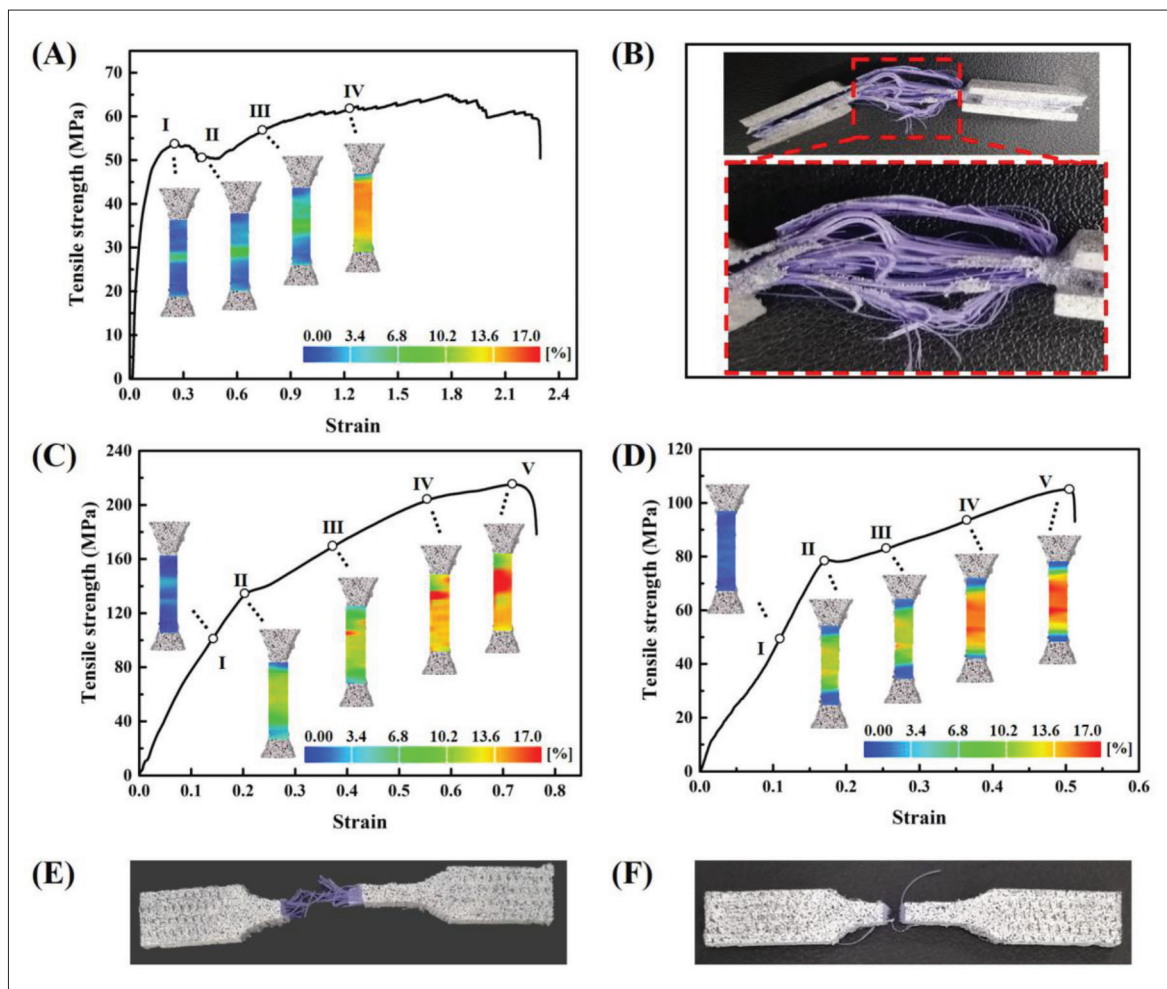


Figure 9. 3D full-field strain measurement system (3DFFSMS) analysis results. (A) Scheme 3, (B) specimen of scheme 3, (C) scheme 4, (D) scheme 6, (E) specimen of scheme 4, and (F) failed specimen of scheme 6.

area, and the area of the red region gradually expanded until the specimen fractured. As shown in Figure 9E, the fracture location of the specimen was consistent with the location of the red stress concentration area at point V on the stress-strain curve. Unlike the specimen of scheme 3, the bonding between the PLA matrix and PGA fibers was good, and no debonding situation occurred until the specimen failed.

The tensile process of the specimen of scheme 6 was similar to that of scheme 4. The stress-strain curves, strain cloud and fractured specimen of scheme 6 are illustrated in Figures 9D and F. In the strain cloud history, the specimen showed lower strain values than that of scheme 4, which means that the tensile strength of the specimen of scheme 6 was inferior to that of scheme 4. The shapes of the stress-strain curves and post-fracture morphologies of specimens of schemes 7 and 8 were similar to those of scheme 6 shown in Figure 9D. The shape of the stress-strain curve of

the specimen of scheme 5 was similar to that of scheme 3 shown in Figure 9A.

3.3. Results of internal defect analysis

The presence of internal porosity defects between deposition lines is a common problem in FDM printing. These internal defects are related to the printing process parameters, which will affect the performance of a printed part. A specimen was randomly selected from each experimental scheme for internal defect analysis. Figure 10 shows the analysis results of the internal defects of the specimens obtained by the micro-X-ray 3D imaging system. Different colors were used to represent the sizes of the internal voids in the figure, and the measured porosities are shown in Table 2. The internal defects of specimens printed with different process parameters were also different. The defects in scheme 3 (Figure 10) were clearly visible, and there were more defects in the upper layer than in the lower layer.

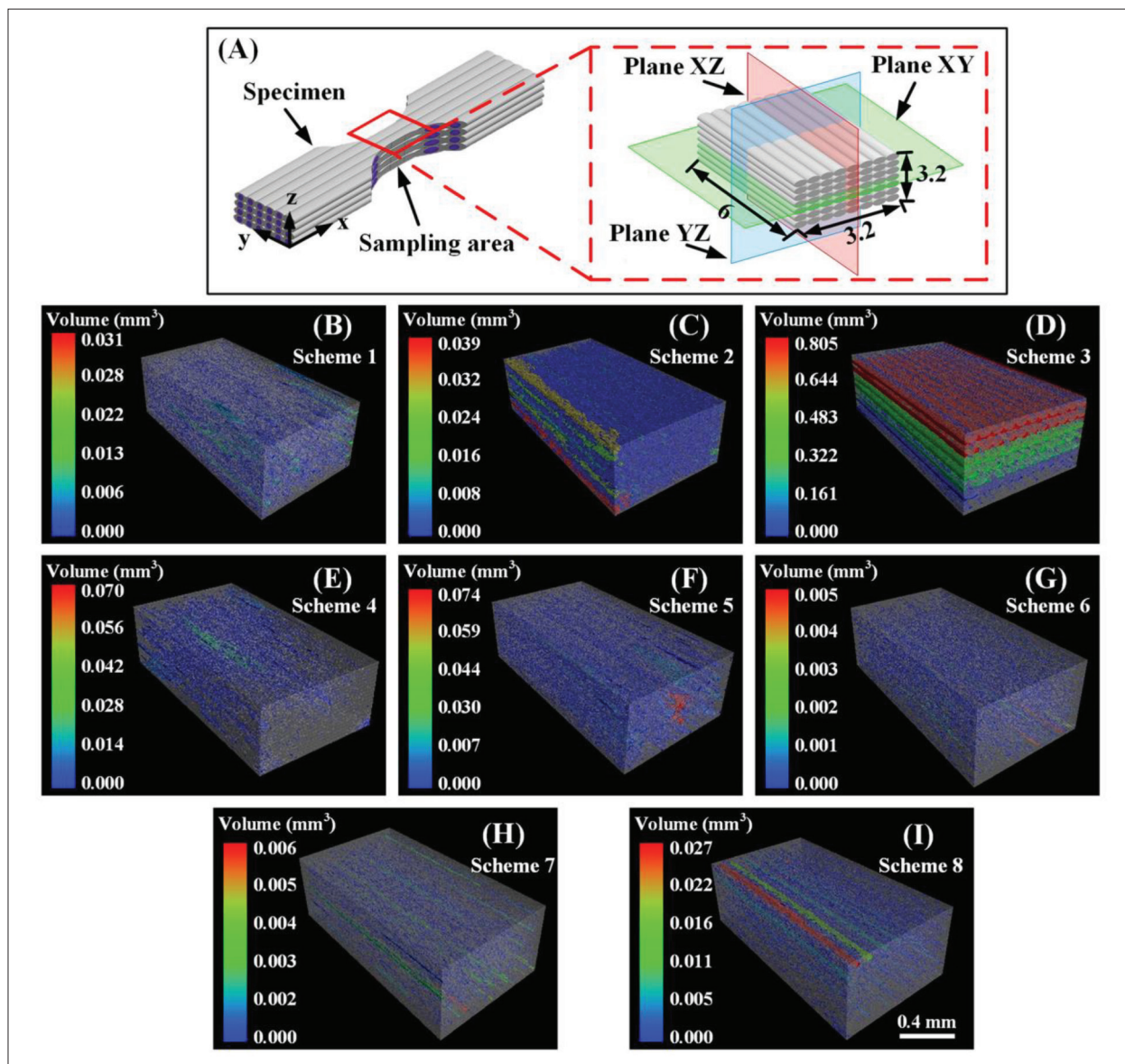


Figure 10. Comparison of internal defects of different schemes. (A) Sampling area for defect analysis and (B–I) internal defect distributions of schemes 1–8.

3.4. Results of morphology analysis

3.4.1. Morphologies of deposited lines

When molten material was extruded from the nozzle onto the hotbed, the flat surface at the bottom of the nozzle exerted pressure on the material, causing it to spread out to the sides^[21]. The distance from the bottom of the nozzle to the hotbed was the thickness of the printed layer. The front perspective of single deposition lines fabricated by different layer thicknesses was captured by the high-speed camera, which is shown at the top of Figure 11. The cross-sections of the single deposition lines are shown at the bottom. The PGA fibers embedded in the PLA matrix in a solid state indicates successful composite printing.

As the layer thickness increased, the cross-section of the single deposition line was gradually changed from a flat shape to a circular shape. At the same time, the embedded fibers also gradually floated upward, which could be seen from both the front and cross-sectional views. When the molten material was extruded from the nozzle, the flat surface at the bottom of the nozzle exerted pressure on the molten material, causing it to spread out to the sides. A smaller layer thickness setting means that the extruded molten material would have a higher extrusion pressure, which facilitated the extension of the material to the sides, ultimately resulting in a flattened deposited cross-section. Conversely, a high printing layer thickness would

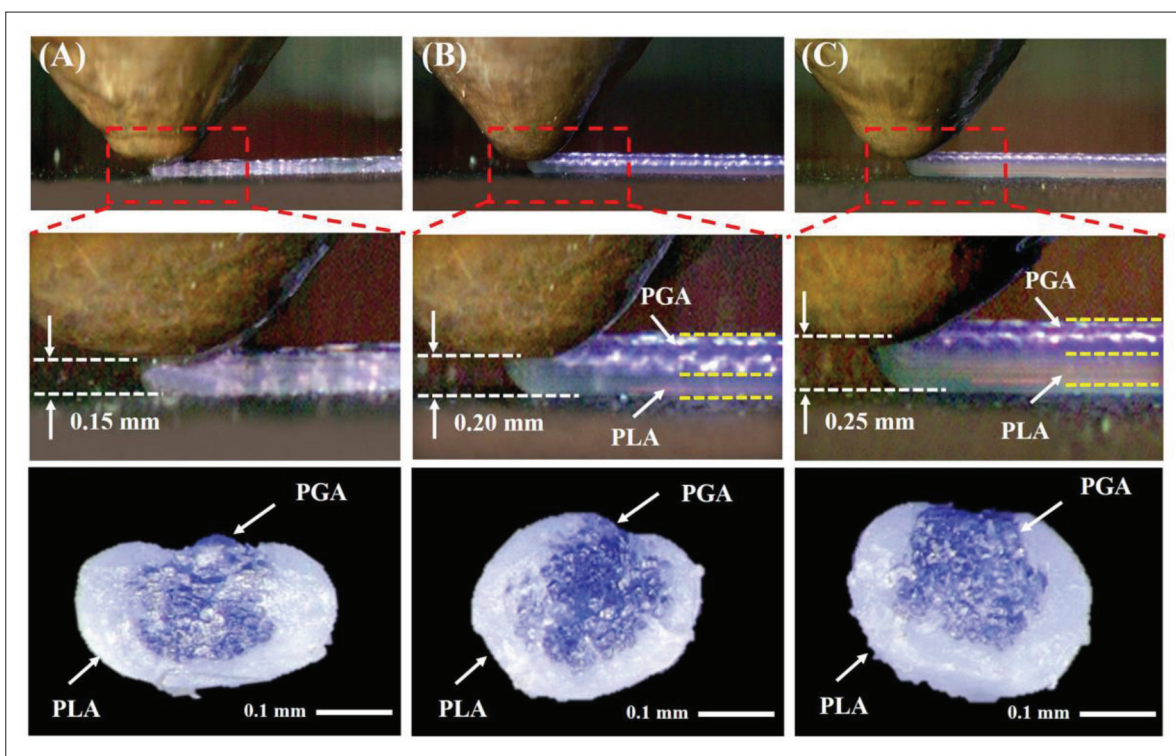


Figure 11. Positions of polyglycolic acid (PGA) fibers in the deposition lines with different layer thicknesses. (A) 0.15 mm, (B) 0.20 mm, and (C) 0.25 mm. Abbreviation: PLA, polylactic acid.

result in a lower extrusion pressure, which would not help the material expand to the sides, ultimately leading to a circular deposition line. Similarly, the loose and soft PGA fibers also required an extrusion pressure to embed them into the molten matrix materials. A smaller layer thickness was more conducive to pressing the fibers into the bottom of the matrix, and the flowing matrix material was more likely to wrap around the fibers. When the printing layer thickness was too large, the PGA fibers could easily float on the surface of the deposition line due to the low extrusion pressure effect of the nozzle. Furthermore, the fibers tended to be pulled out during the printing process, resulting in printing failure when the layer thickness was too large.

3.4.2. Morphologies of cross-sections of specimens

Figure 12 shows cross-sectional photographs of the specimens with layer thicknesses of 0.15, 0.2, and 0.25 mm. The cross-sectional surface of each specimen was polished with 1200-mesh sandpaper and then treated with the ultrasonic cleaner to clean the surface and the residual material in the crevasses. When the layer thickness was 0.15 mm (Figure 12A), the combination of the deposited lines was very tight, the PGA fibers were pressed into an inverted trapezoid and embedded well in the PLA matrix, and the fine PGA fibers were also pressed closely. When the

layer thickness was 0.2 mm (Figure 12B), the PGA fibers also showed an inverted trapezoid shape, but the trapezoid height was slightly higher and the fine fibers were loose. When the layer thickness was 0.25 mm (Figure 12C), there were distinct gaps between the deposition lines, and the sections of the PGA fibers were approximately circular. There were also distinct gaps between the fine fibers of the PGA fiber bundle, indicating that the compaction effect of the nozzle bottom surface on the extruded material was not significant.

3.4.3. Fracture analysis

Figure 13 shows the cross-sectional FESEM images of the fractured specimens printed by schemes 6, 7, and 8, for which the printing speeds were 7 mm/s (Figure 13A), 8 mm/s (Figure 13B), and 9 mm/s (Figure 13C), respectively. There were no significant differences in the cross-sectional morphologies of the specimens printed at different printing speeds. The PGA fibers were well bonded to the matrix, without many fibers being pulled out. However, when the printing speed increased from 7 to 9 mm/s, the widths of the single deposition lines became narrow, and overlapping voids between two adjacent deposition lines formed. When the printing speed was 9 mm/s, the deposition lines were relatively narrow, and the voids between deposition lines were relatively large.

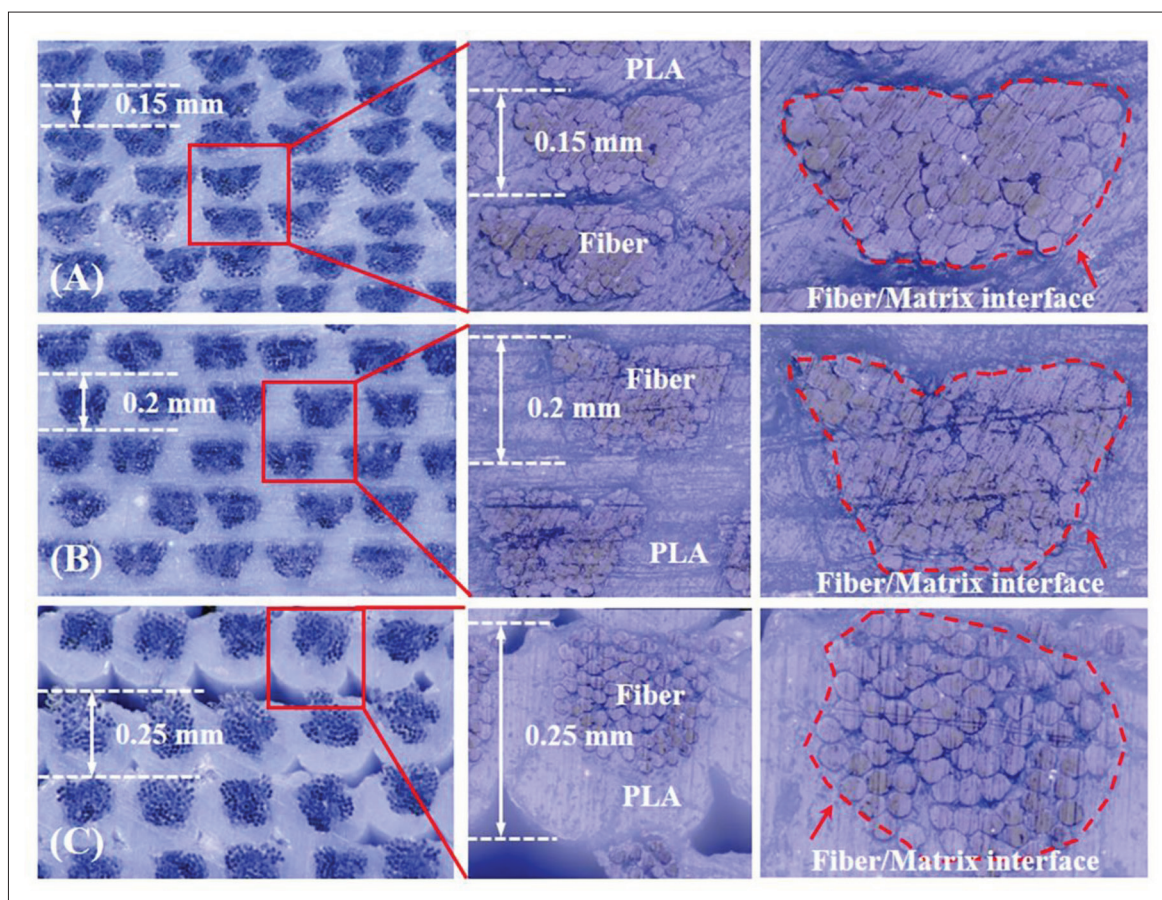


Figure 12. Cross-sectional morphologies of specimens with different layer thicknesses. (A) 0.15 mm, (B) 0.20 mm, and (C) 0.25 mm. Abbreviations: PGA, polyglycolic acid; PLA, polylactic acid.

4. Discussion

Table 2 shows the cross-sections, fiber quantities, fiber contents, porosities, and tensile strengths of the specimens made by each scheme. The experimental results showed that the specimen with the largest tensile strength was from scheme 4, which had the largest number of fibers, the highest fiber content, and the lowest porosity. The worst tensile properties were obtained from scheme 3, because the fiber contents of this specimen were low and the porosity was the largest of the specimens from all schemes.

In a composite specimen, the fibers play a key role in bearing an external load, and the matrix transfers the load. Therefore, a reasonably high fiber content means that the specimen can bear more load and exhibit a high tensile strength. The parts printed by FDM were formed by the accumulation of numerous PLA/PGA deposition lines. When a part contained more deposition lines, its fiber content was higher. To increase the number of deposition lines, it was necessary to reduce the spacing of the deposition lines and increase the number of layers.

For the same volume of the part, the fiber content was needed to be increased by reducing the printing space of the deposition line and the thickness of each layer. Scheme 4 had the smallest printing space and layer thickness, so its fiber content was the highest among all the schemes, and the tensile strength of the specimen was the highest.

Scheme 3 had the lowest tensile strength because the specimen was printed by the maximum layer thickness (0.25 mm), resulting in a low fiber number (130) and fiber content (37.0%). Compared with scheme 8 with the lowest fiber number (128) and fiber content (36.5%), scheme 3 only had two more fibers (130). However, the porosity of the specimen printed in scheme 3 was 7.5 times that of the specimen printed in scheme 8. The specimen in scheme 3 showed an inferior tensile strength to that of scheme 8, even though the specimen in scheme 3 had a larger fiber content. According to the porosity analysis shown in Figure 10D, there were many voids in the specimen, the void distribution was uneven, and the defects in the upper part of the sample were more evident. The cross-section in Figure 12 also shows a distinct interlayer gap, indicating

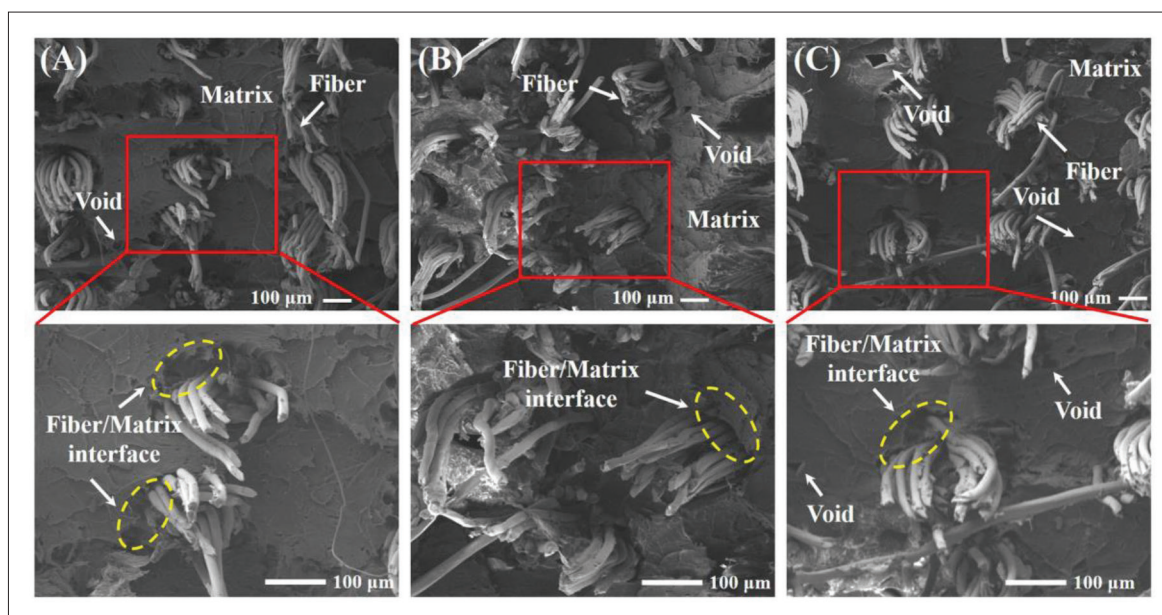


Figure 13. Field emission scanning electron microscopy (FESEM) images of fractures of specimens with different printing speeds. (A) 7 mm/s, (B) 8 mm/s, and (C) 9 mm/s.

that the materials between two adjacent layers were not fully fused. The gaps and voids between layers hindered the heat from the hotbed from conducting upward. They also affected the fusion between deposition lines, further causing more defects in the upper part, as shown in Figure 10D. The poor bonding quality between interlayers also caused the layers to debond easily during the tensile process. As shown in Figure 9B, many fibers were exposed after the matrix fell off.

The volume of a printed specimen was made up of three parts: fibers, matrix material, and pores. The printing speed and filament feeding speed affected the extrusion amount of the PLA and further affected the morphology of a single deposition line. Using a slow printing speed, the extruded amount of PLA increased. A slow printing speed could increase the extrusion amount of PLA, make the shape of a single deposition line flatter, and help to reduce the porosity. If a specimen was printed with the same printing layer thickness and printing space conditions, the fiber content would remain constant. However, by changing the printing speed, the extruded amount of PLA changed, further affecting the porosities and tensile strengths of the printed specimens.

In the process parameter selection test, when the layer thickness was set to 0.1 mm, the PGA fibers were easy to break. When the printing speed exceeded 9 mm/s, PGA fibers were also easy to break and easily pulled out of the matrix when the printing direction changed. When the printing temperature exceeded 220°C, PGA fibers were also very easy to break.

Figure 14 shows the effects of the layer thickness and print spacing on the porosity, fiber content, and tensile strength. There was a positive correlation between the tensile strength of the specimen and the fiber content. Conversely, the porosity had a negative influence on the tensile strengths of the printed specimens.

To evaluate the effect of the PGA fiber reinforcement, three pure PLA tensile specimens were printed. The printing parameters were the same as those in scheme 4, and the tensile strength was 37.61 ± 3.37 MPa. The tensile strength of PLA specimen reinforced with PGA fiber was significantly improved, and the tensile strength of PLA/PGA composite specimen was 5.6 times that of PLA specimen.

The printing process parameters of PLA/PGA composites are quite different from those of PLA and PLA/HA materials. The main reasons are to ensure that: (i) PGA fiber is not broken after adding PGA fiber, (ii) the layer thickness is not less than the diameter of the fiber, and (iii) the fiber can be pulled out of the nozzle smoothly by reducing the printing speed.

Because the nozzle outlet diameter is 0.4 mm and the fiber diameter is 0.15 mm, the filament feeding speed becomes slower. If the filament feeding speed is slightly faster, the molten PLA material will overflow from the inlet hole of the PGA fiber, and if the filament feeding speed is slightly slower, the connection between fibers will not be reliable.

Schemes 6, 7, and 8 adopt the filament feeding speed of 0.2 mm/s, because when the layer thickness is 0.2 mm, the

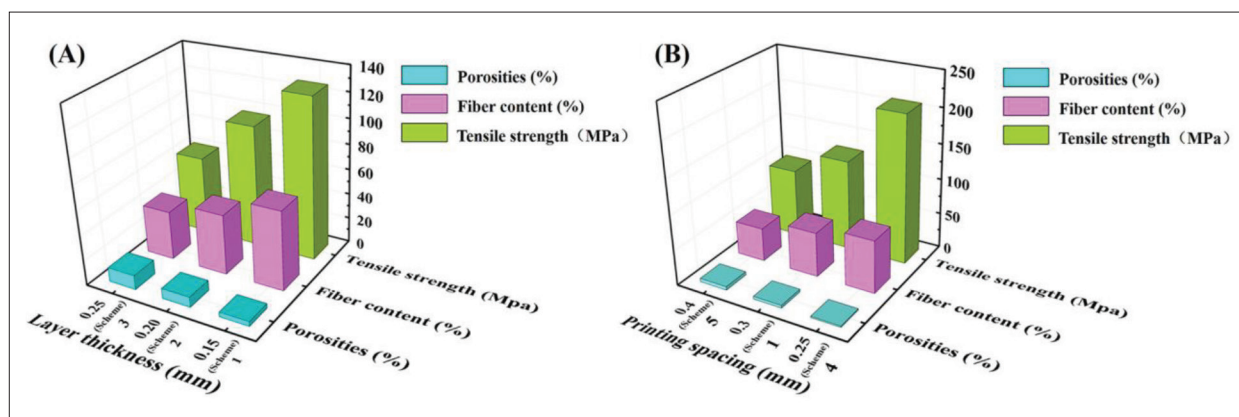


Figure 14. Influence of print layer thickness and print spacing on porosity, fiber content, and tensile strength according to (A) different layer thicknesses and (B) different print spacings.

Table 3. Tensile strengths of fused deposition modeling (FDM) polymer materials and composites

Materials	Reinforcement method	Tensile strength (MPa)
PLA (this work)	-	37.60
PEEK ^[42]	-	95.21
CFR-PEEK ^[42]	Short fiber	101.41
PCL/PGA ^[39]	Continuous fiber	79.70
PLA/PGA (this work)	Continuous fiber	209.32
Cortical bone ^[43]	-	60–160

Abbreviations: CFR-PEEK, carbon-fiber-reinforced polyether ether ketone; PCL, poly (ε-caprolactone); PEEK, polyether ether ketone; PGA, polyglycolic acid; PLA, polylactic acid.

deposited line printed at the original set filament feeding speed of 0.1 mm/s does not connect well, and it is necessary to improve the connection between deposited lines by accelerating the filament feeding speed. Based on the above reasons, this study did not further analyze the influence of filament feeding speed on mechanical properties.

Table 3 summarizes the tensile strengths of common polymer materials and polymer-based composites reported in the literature. The tensile strengths (along the fiber direction) of the specimens printed in seven schemes were superior to that of PEEK^[42], the tensile strengths (along the fiber direction) of the specimens printed in four schemes were superior to that of carbon-fiber-reinforced (CFR) PEEK^[42], and all eight schemes reached or exceeded the cortical tensile strength^[43]. Moreover, the printing process parameters could be adjusted to change the fiber content and porosity to obtain implants with different tensile strengths to match different strength requirements. Therefore, the continuous PGA fiber-reinforced PLA composites proposed in this study have good potential for use in load-bearing degradable bone implants.

In this work, single-factor experiments were used to investigate the influence of four process parameters on the mechanical properties of PLA/PGA composites. However, the effect of the combination of multiple process parameters on the mechanical properties of the printed part cannot be well revealed by the single-factor experiment. On the basis of this study, multi-factor and multi-level process parameter experiments by orthogonal experiments are warranted in future studies, and the relationship between the process parameters and the mechanical properties of the printed part should be investigated to determine the optimal process parameters.

5. Conclusion

In summary, the 3D-printed continuous PGA fiber-reinforced PLA composite specimens showed good mechanical properties. The main conclusions of this work are as follows:

The tensile strength of the specimen was related to its fiber content and porosity. The specimens with high fiber contents and low porosities had high tensile strengths. The printing layer thickness and printing spacing had significant impacts on the fiber content. The printing speed did not affect fiber content but had a slight effect on the tensile strength. Different fiber contents could be obtained by choosing different printing spacings and layer thicknesses, and then parts with different tensile strengths could be obtained.

The tensile strength (along the fiber direction) of the specimen with the highest tensile strength was 209.32 ± 8.37 MPa, and its fiber content and porosity were 77.8% and 1.82%, respectively. This tensile strength was higher than those of cortical bone, PEEK, and short-fiber-reinforced PEEK, indicating that the continuous PGA fiber-reinforced PLA composites have great potential

for the manufacture of biodegradable load-bearing bone implants.

Acknowledgments

None.

Funding

This work was supported by the Natural Science Foundation of Xinjiang, China (grant number 2022D01C393).

Conflict of interest

The authors declare no conflict of interest.

Author contributions

Conceptualization: Patiguli Aihemaiti, Ru Jia

Investigation: Patiguli Aihemaiti, Ru Jia, Houfeng Jiang, Ayiguli Kasimu

Supervision: Wurikaixi Aiyiti

Writing – original draft: Patiguli Aihemaiti, Ru Jia

Writing – review & editing: Patiguli Aihemaiti, Ru Jia, Wurikaixi Aiyiti

Ethics approval and consent to participate

Not applicable.

Consent for publication

Not applicable.

Availability of data

Data can be obtained from the corresponding author upon reasonable request.

References

- Javaid M, Haleem A, 2018, Additive manufacturing applications in orthopaedics: A review. *J Clin Orthop Trauma*, 9(3):202–206.
<https://doi.org/10.1016/j.jcot.2018.04.008>
- Rony L, Lancigu R, Hubert L, 2018, Intraosseous metal implants in orthopedics: A review. *Morphologie*, 102(339):231–242.
<https://doi.org/10.1016/j.morpho.2018.09.003>
- Tong Y, Kaplan DJ, Spivak JM, *et al.*, 2020, Three-dimensional printing in spine surgery: A review of current applications. *Spine J*, 20(6):833–846.
<https://doi.org/10.1016/j.spinee.2019.11.004>
- Li C, Pisignano D, Zhao Y, *et al.*, 2020, Advances in medical applications of additive manufacturing. *Engineering*, 6(11):1222–1231.
<https://doi.org/10.1016/j.eng.2020.02.018>
- Kaur M, Singh K, 2019, Review on titanium and titanium based alloys as biomaterials for orthopaedic applications. *Mater Sci Eng C*, 102:844–862.
<https://doi.org/10.1016/j.msec.2019.04.064>
- Chen CH, Chang WJ, Chen YS, *et al.*, 2022, Development of a novel hybrid suture anchor for osteoporosis by integrating titanium 3D printing and traditional machining. *Int J Bioprint*, 8(4):608.
<https://doi.org/10.18063/ijb.v8i4.608>
- Wang F, Chen H, Yang P, *et al.*, 2020, Three-dimensional printed porous tantalum prosthesis for treating inflammation after total knee arthroplasty in one-stage surgery: A case report. *J Int Med Res*, 48(3):300060519891280.
<https://doi.org/10.1177/0300060519891280>
- Bandyopadhyay A, Mitra I, Shivaram A, *et al.*, 2019, Direct comparison of additively manufactured porous titanium and tantalum implants towards in vivo osseointegration. *Addit Manuf*, 28:259–266.
<https://doi.org/10.1016/j.addma.2019.04.025>
- Haleem A, Javaid M, 2019, Polyether ether ketone (PEEK) and its 3D printed implants applications in medical field: An overview. *Clin Epidemiol Global Health*, 7(4):571–577.
<https://doi.org/10.1016/j.cegh.2019.01.003>
- Liu D, Fu J, Fan H, *et al.*, 2018, Application of 3D-printed PEEK scapula prosthesis in the treatment of scapular benign fibrous histiocytoma: A case report. *J Bone Oncol*, 12:78–82.
<https://doi.org/10.1016/j.jbo.2018.07.012>
- Manam NS, Harun WSW, Shri DNA, *et al.*, 2017, Study of corrosion in biocompatible metals for implants: A review. *J Alloys Compd*, 701:698–715.
<https://doi.org/10.1016/j.jallcom.2017.01.196>
- Chen Z, Chen Y, Ding J, *et al.*, 2023, Blending strategy to modify PEEK-based orthopedic implants. *Compos Part B Eng*, 250:110427.
<https://doi.org/10.1016/j.compositesb.2022.110427>
- Baptista R, Guedes M, 2021, Morphological and mechanical characterization of 3D printed PLA scaffolds with controlled porosity for trabecular bone tissue replacement. *Mater Sci Eng C Mater Biol Appl*, 118:111528.
<https://doi.org/10.1016/j.msec.2020.111528>
- Saniei H, Mousavi S, 2020, Surface modification of PLA 3D-printed implants by electrospinning with enhanced bioactivity and cell affinity. *Polymer*, 196:122467.
<https://doi.org/10.1016/j.polymer.2020.122467>
- Myers D, Abdel-Wahab A, Hafeez F, *et al.*, 2022, Optimisation of the additive manufacturing parameters of polylactic acid (PLA) cellular structures for biomedical applications. *J Mech Behav Biomed Mater*, 136:105447.
<https://doi.org/10.1016/j.jmbbm.2022.105447>

16. Wang X, Jiang M, Zhou Z, *et al.*, 2017, 3D printing of polymer matrix composites: A review and prospective. *Compos Part B Eng*, 110:442–458.
<https://doi.org/10.1016/j.compositesb.2016.11.034>
17. Ilyas RA, Sapuan SM, Harussani MM, *et al.*, 2021, Polylactic acid (PLA) biocomposite: Processing, additive manufacturing and advanced applications. *Polymers (Basel)*, 13(8):1326.
<https://doi.org/10.3390/polym13081326>
18. Zhao X, Liu J, Li J, *et al.*, 2022, Strategies and techniques for improving heat resistance and mechanical performances of poly(lactic acid) (PLA) biodegradable materials. *Int J Biol Macromol*, 218:115–134.
<https://doi.org/10.1016/j.ijbiomac.2022.07.091>
19. Backes EH, Fernandes EM, Diogo GS, *et al.*, 2021, Engineering 3D printed bioactive composite scaffolds based on the combination of aliphatic polyester and calcium phosphates for bone tissue regeneration. *Mater Sci Eng C Mater Biol Appl*, 122:111928.
<https://doi.org/10.1016/j.msec.2021.111928>
20. Zhang H, Mao X, Du Z, *et al.*, 2016, Three dimensional printed macroporous polylactic acid/hydroxyapatite composite scaffolds for promoting bone formation in a critical-size rat calvarial defect model. *Sci Technol Adv Mater*, 17(1):136–148.
<https://doi.org/10.1080/14686996.2016.1145532>
21. Aihemaiti P, Jiang H, Aiyiti W, *et al.*, 2022, Optimization of 3D printing parameters of biodegradable polylactic acid/hydroxyapatite composite bone plates. *Int J Bioprint*, 8(1):153–166.
<https://doi.org/10.18063/ijb.v8i1.490>
22. Zhang B, Wang L, Song P, *et al.*, 2021, 3D printed bone tissue regenerative PLA/HA scaffolds with comprehensive performance optimizations. *Mater Des*, 201:109490.
<https://doi.org/10.1016/j.matdes.2021.109490>
23. Wang W, Zhang B, Li M, *et al.*, 2021, 3D printing of PLA/n-HA composite scaffolds with customized mechanical properties and biological functions for bone tissue engineering. *Compos Part B Eng*, 224(1):109192.
<https://doi.org/10.1016/j.compositesb.2021.109192>
24. Maqsood N, Rimašauskas M, 2021, Delamination observation occurred during the flexural bending in additively manufactured PLA-short carbon fiber filament reinforced with continuous carbon fiber composite. *Results Eng*, 11:100246.
<https://doi.org/10.1016/j.rineng.2021.100246>
25. Dou H, Cheng Y, Ye W, *et al.*, 2020, Effect of process parameters on tensile mechanical properties of 3D printing continuous carbon fiber-reinforced PLA composites. *Materials (Basel)*, 13(17):3850.
<https://doi.org/10.3390/ma13173850>
26. Ali W, Mehboob A, Han M-G, *et al.*, 2020, Novel biodegradable hybrid composite of polylactic acid (PLA) matrix reinforced by bioactive glass (BG) fibres and magnesium (Mg) wires for orthopaedic application. *Compos Struct*, 245:112322.
<https://doi.org/10.1016/j.compstruct.2020.112322>
27. Wang G, Zhang D, Li B, *et al.*, 2019, Strong and thermal-resistance glass fiber-reinforced polylactic acid (PLA) composites enabled by heat treatment. *Int J Biol Macromol*, 129:448–459.
<https://doi.org/10.1016/j.ijbiomac.2019.02.020>
28. Long Y, Zhang Z, Fu K, *et al.*, 2021, Efficient plant fibre yarn pre-treatment for 3D printed continuous flax fibre/poly(lactic) acid composites. *Compos Part B Eng*, 227:109389.
<https://doi.org/10.1016/j.compositesb.2021.109389>
29. Baley C, Bourmaud A, Davies P, 2021, Eighty years of composites reinforced by flax fibres: A historical review. *Compos Part A Appl Sci Manuf*, 144:106333.
<https://doi.org/10.1016/j.compositesa.2021.106333>
30. Akmal Zia A, Tian X, Liu T, *et al.*, 2023, Mechanical and energy absorption behaviors of 3D printed continuous carbon/Kevlar hybrid thread reinforced PLA composites. *Compos Struct*, 303:116386.
<https://doi.org/10.1016/j.compstruct.2022.116386>
31. Tian X, Todoroki A, Liu T, *et al.*, 2022, 3D printing of continuous fiber reinforced polymer composites: Development, application, and prospective. *CJME:AM*, 001(001):50–69.
<https://doi.org/10.1016/j.cjmeam.2022.100016>
32. Kabir SMF, Mathur K, Seyam A-FM, 2020, A critical review on 3D printed continuous fiber-reinforced composites: History, mechanism, materials and properties. *Compos Struct*, 232:111476.
<https://doi.org/10.1016/j.compstruct.2019.111476>
33. Maqsood N, Rimašauskas M, 2021, Characterization of carbon fiber reinforced PLA composites manufactured by fused deposition modeling. *Compos Part C*, 4:100112.
<https://doi.org/10.1016/j.jcomc.2021.100112>
34. Tian X, Liu T, Yang C, *et al.*, 2016, Interface and performance of 3D printed continuous carbon fiber reinforced PLA composites. *Compos Part A Appl Sci Manuf*, 88: 198–205.
<https://doi.org/10.1016/j.compositesa.2016.05.032>
35. Hou Z, Tian X, Zheng Z, *et al.*, 2020, A constitutive model for 3D printed continuous fiber reinforced composite structures with variable fiber content. *Composites Part B Eng*, 189:107893.
<https://doi.org/10.1016/j.compositesb.2020.107893>

36. Hedayati SK, Behraves AH, Hasannia S, *et al.*, 2022, Additive manufacture of PCL/nHA scaffolds reinforced with biodegradable continuous fibers: Mechanical properties, in-vitro degradation profile, and cell study. *Eur Polym J*, 162:110876.
<https://doi.org/10.1016/j.eurpolymj.2021.110876>
37. Takayama T, Daigaku Y, Ito H, *et al.*, 2014, Mechanical properties of bio-absorbable PLA/PGA fiber-reinforced composites. *J Mech Sci Technol*, 28(10):4151–4154.
<https://doi.org/10.1007/s12206-014-0927-3>
38. Ko HS, Lee S, Lee D, *et al.*, 2021, Mechanical properties and bioactivity of poly(lactic acid) composites containing poly(glycolic acid) fiber and hydroxyapatite particles. *Nanomaterials (Basel)*, 11(1):249.
<https://doi.org/10.3390/nano11010249>
39. Hedayati SK, Behraves AH, Hasannia S, *et al.*, 2020, 3D printed PCL scaffold reinforced with continuous biodegradable fiber yarn: A study on mechanical and cell viability properties. *Polym Test*, 83:106347.
<https://doi.org/10.1016/j.polymertesting.2020.106347>
40. Rodríguez-Reyna SL, Mata C, Díaz-Aguilera JH, *et al.*, 2022, Mechanical properties optimization for PLA, ABS and Nylon + CF manufactured by 3D FDM printing. *Mater Today Commun*, 33:104774.
<https://doi.org/https://doi.org/10.1016/j.mtcomm.2022.104774>
41. Liu Z, Lei Q, Xing S, 2019, Mechanical characteristics of wood, ceramic, metal and carbon fiber-based PLA composites fabricated by FDM. *J Mater Res Technol*, 8(5):3741–3751.
<https://doi.org/10.1016/j.jmrt.2019.06.034>
42. Han X, Yang D, Yang C, *et al.*, 2019, Carbon fiber reinforced PEEK composites based on 3D-printing technology for orthopedic and dental applications. *J Clin Med*, 8(2):240.
<https://doi.org/10.3390/jcm8020240>
43. Vlasea M, Basalah A, Azhari A, *et al.*, (eds), 2015, Chapter 11: Additive manufacturing for bone load bearing applications, in *3D Bioprinting and Nanotechnology in Tissue Engineering and Regenerative Medicine (Second Edition)*, Academic Press, 231–263.